

Article 3 :

Publié dans la revue : *Journal of the Brazilian Society of Mechanical Sciences and Engineering*.

- **Éditeur** : Springer Nature (Berlin/Heidelberg)
- **ISSN** : **1678-5878** **E-ISSN** : **1806-3691**
- **Lien article DOI** : <https://doi.org/10.1007/s40430-025-05812-6>
- **Période de couverture par Scopus** : de 2003 à 2025
- **Domaines scientifiques** : Génie civil ; Mathématiques (Mathématiques générales)
- **Impact facture** : **2.1 (2024)** ;
- **Type de source** : Revue classée A (*lien* :
https://www.dgrstd.dz/fr/revues_A?search=Journal+of+the+Brazilian+Society+of+Mechanical+Sciences+and+Engineering



Revues & publications scientifiques

Moteur de recherche - Revues scientifiques

Journal of the Brazilian Society of Mechanical Sciences and Engineering

Résultat : 1

Télécharger

TITRE DE LA REVUE--	EDITEUR	ISSN	EISSN
JOURNAL OF THE BRAZILIAN SOCIETY OF MECHANICAL SCIENCES AND ENGINEERING	SPRINGER HEIDELBERG	1678-5878	1806-3691

Static, free vibration, and buckling analysis of functionally graded plates using strain approach and Reissner–Mindlin elements

Review Paper | Published: 08 August 2025

Volume 47, article number 498, (2025) [Cite this article](#)



[Journal of the Brazilian Society of Mechanical Sciences and Engineering](#)

[Aims and scope](#) →

[Submit manuscript](#) →

Taqiyeddine Assas Messaoud Bourezane & Madjda Chenafi

94 Accesses [Explore all metrics](#) →

[Access this article](#)

[Log in via an institution](#) →



Check for updates

Cite this article

Assas, T., Bourezane, M. & Chenafi, M. Static, free vibration, and buckling analysis of functionally graded plates using strain approach and Reissner–Mindlin elements. *J Braz. Soc. Mech. Sci. Eng.* **47**, 498 (2025). <https://doi.org/10.1007/s40430-025-05812-6>

[Download citation](#)

Received

18 February 2024

Accepted

09 July 2025

Published

08 August 2025

DOI

<https://doi.org/10.1007/s40430-025-05812-6>

Keywords

[Static](#)

[Free vibration](#)

[Buckling analysis](#)

[Reissner–Mindlin](#)

[Functionally graded](#)

[Strain based](#)



Static, free vibration, and buckling analysis of functionally graded plates using strain approach and Reissner–Mindlin elements

Taqiyeddine Assas¹ · Messaoud Bourezane¹ · Madjda Chenaf¹

Received: 18 February 2024 / Accepted: 9 July 2025 / Published online: 8 August 2025

© The Author(s), under exclusive licence to The Brazilian Society of Mechanical Sciences and Engineering 2025

Abstract

The novelty of the present work lies in the development of a new four-node rectangular finite element using strain-based and Reissner–Mindlin theory. This paper is the first to apply this innovative approach to study the static, free vibration, and buckling responses of functionally graded materials (FGMs) plates. The mechanical properties of the FGM plate are considered to vary along the thickness direction by the power-law distributions. The notion of a neutral surface has been used to prevent the stretching–bending effect. The developed element has six degrees of freedom (DOFs) per node, obtained by combining two strain-based elements. The first one is a membrane which has three DOFs per node, and the second one is a Reissner–Mindlin plate which has three DOFs per node. The displacement fields of these components are represented by higher-order expressions based on the strain approach, which satisfy both rigid body modes and compatibility equations. The performance of the proposed element is evaluated through various numerical problems, and the results are compared with those published in the literature, showing good agreement. The impact of the gradient index, side-to-thickness ratio, aspect ratio, and loading types on the stresses, transverse displacements, frequency response, and critical buckling load of FGM plates is also investigated and discussed.

Keywords Static · Free vibration · Buckling analysis · Reissner–Mindlin · Functionally graded · Strain based

1 Introduction

In recent decades, the notion of functionally graded materials (FGM) has emerged from the work of a Japanese scientist in 1984 [1], which are used in industrial environments due to their excellent performance compared to conventional materials. FGM is a family of composite inhomogeneous materials consisting of a combination of isotropic materials, generally ceramics and metals, and it has many advantages, including progressive and continuous changes in their mechanical and thermal characteristics across the thickness, which prevents problems associated with traditional laminated composite structures, like higher inter-laminar stresses between the layers of a composite laminate [2].

As a result, these materials are attracting significant attention in various engineering disciplines, such as aerospace, mechanical, automotive, civil, and biomedical engineering. Many researches have been studied for static, free vibrational, and buckling behaviors of FGM beams, plates, and shells using several analytical and numerical approaches, relying on various theories, including classical plate theory (CPT), which neglects the effects of transverse shear deformation [3–7], first-order shear deformation theory (FSDT) having a linear variation in displacements [8–12], and higher-order shear deformation theory (HSDT) involving higher-order variations in displacements across the plate thickness, such as third-order shear deformation plate theory (TSDT), sinusoidal shear deformation plate theory (SSDT), and hyperbolic shear deformation plate theory (HDT) [13–23].

Several developers have employed the strain approach to design finite elements that are both efficient and durable. Initially, Ashwell et al. [24] introduced this methodology specifically for curved elements. Subsequently, this approach was employed in the analysis of shell structures [25–27]. It was later expanded to encompass plane-elasticity elements

Technical Editor: Samikkannu Raja.

✉ Taqiyeddine Assas
taqiyeddine.assas@univ-biskra.dz

¹ Hydraulic and Environmental Development Laboratory (LAHE), Department of Civil and Hydraulic Engineering, University of Biskra, Biskra, Algeria

[28–30] and further extended to address 3D elasticity problems [31–33]; the method was also applied to plate bending [34–39]. It is important to observe that all previously formulated plate elements using the strain approach were designed specifically for isotropic materials. Thus, the researchers were motivated to develop a new finite element using the strain approach for the analysis of FG plates.

The primary objective of the current work is to contribute to the modeling of static, free vibration, and mechanical buckling of functionally graded material (FGM) plates by developing, for the first time, a new four-node rectangular element based on the strain approach and Reissner–Mindlin plate theory. The material characteristics of FGM plates, such as Young's modulus and density, are considered to vary continuously throughout the thickness of the plate with a power-law function of the volume fraction of the components, while the Poisson's ratio remains constant. To prevent the membrane-bending coupling, the notion of physical neutral surface has been presented. The developed element called SBRP24 (Strain-Based Rectangular Plate with 24 degrees of freedom) has six degrees of freedom ($u, v, \theta_z, w, \beta_x, \beta_y$) for each node, and their displacement fields are derived by combining membrane and bending elements based on the strain approach. The membrane element, called SBRIEIR (Strain-Based Rectangular In-Plane Elasticity In-Plane Rotation), developed by Sabir [30], having three degrees of freedom at each node, two translations (u, v) and one in-plane rotation (θ_z), while the bending element, named SBRP (Strain-Based Rectangular Plate), developed by Belounar and Guenfoud [37], has three DOFs (w, β_x, β_y) per node. Additionally, the potential energy and Hamilton's principle are applied to obtain the stiffness, mass, and geometrical matrices. Different numerical problems are studied and analyzed to evaluate the efficiency and performance of the current element in predicting the bending, free vibration, and buckling behavior of FGM plates. Furthermore, another objective of this paper is to investigate the impact of several parameters on the behavior of the FGM plate, including the gradient index (p), the side-to-thickness ratio (l/h), the types of loading (sinusoidal or uniformly distributed lateral loads, biaxial and uniaxial compression loads), the aspect ratio (L/l), etc.

2 Theoretical formulation

2.1 FGM plate

Consider a rectangular plate of heterogeneous elastic FGM with length l , width L , and thickness h . It comprises of ceramic material on the upper surface and metallic material on the lower surface, as illustrated in Fig. 1. The material characteristics ($E; \rho$) of the plate change gradually in the

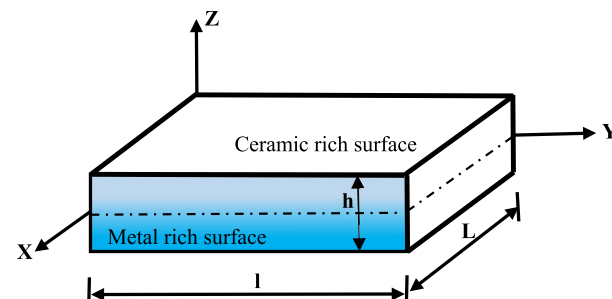


Fig. 1 FG rectangular plate geometry

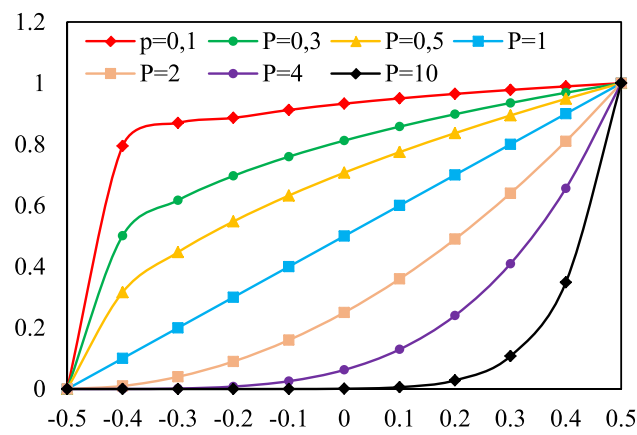


Fig. 2 Variations in the volume proportion (V_c) through the thickness of the FGM plate

direction of thickness, characterized by the power function (P-FGM), as shown in Fig. 2:

$$V_c(z) = \left(\frac{Z}{h} + \frac{1}{2} \right)^p \quad (1)$$

$$P(z) = P_m + (P_c - P_m)V_c(z) \quad (2)$$

where the indicators m and c describe the metal and ceramic, respectively; P_c and P_m are the corresponding material characteristics, such as density (ρ), Young's modulus (E), and other characteristics. ($p \geq 0$) represents the gradient index of martial FGM.

2.2 Limitations and basic assumptions

The assumptions of the current theory are as follows:

- The origin of the Cartesian coordinate system is defined at the neutral surface of the FGM plate.
- The displacement function within the element is approximated using polynomial functions based on the strain

approach, which satisfies both rigid body modes and compatibility equations ("see Appendix").

- Transverse normal stress (σ_z) is assumed to be negligible compared to the in-plane stresses σ_x and σ_y
- Small deformations are assumed, meaning that the displacements are small relative to the thickness of the plate, resulting in infinitesimal strains.

2.3 Displacement functions and strains

The displacement functions of the conventional FSDT are represented by:

$$\begin{aligned} U(x, y, z) &= u(x, y) + z\beta_x(x, y)V(x, y, z) \\ &= v(x, y) + z\beta_y(x, y)W(x, y, z) \\ &= w(x, y)\theta_z(x, y, z) = \theta_z(x, y) \end{aligned} \quad (3)$$

U, V, and W denote the displacements of each point in the (x,y,z) coordinate system; u, v and w are mid-plane displacements. β_x , β_y , and θ_z represent the rotations in yz, xz, and xy planes, respectively.

The drilling rotation θ_z is defined by the following [40]:

$$\theta_z(x, y) = \frac{1}{2} \left(\frac{\partial v(x, y)}{\partial x} - \frac{\partial u(x, y)}{\partial y} \right) \quad (4)$$

The relations between displacement and strain for the FGM plate are defined as follows:

$$\boldsymbol{\varepsilon} = \begin{Bmatrix} \varepsilon_x \\ \varepsilon_y \\ \gamma_{xy} \end{Bmatrix} = \{\varepsilon_m\} + z\{k\} + \{\varepsilon^{nl}\} \quad (5)$$

where

$$\{\varepsilon_m\} = \begin{Bmatrix} \varepsilon_x^0 \\ \varepsilon_{xx}^0 \\ \varepsilon_{yy}^0 \\ \gamma_{xy}^0 \end{Bmatrix} = \begin{Bmatrix} \frac{\partial u}{\partial x} \\ \frac{\partial v}{\partial y} \\ \left(\frac{\partial u}{\partial y} + \frac{\partial v}{\partial x} \right) \end{Bmatrix} \text{(Membrane strains)} \quad (6)$$

$$\{k\} = \begin{Bmatrix} k_{xx} \\ k_{yy} \\ k_{xy} \end{Bmatrix} = \begin{Bmatrix} \frac{\partial \beta_x}{\partial x} \\ \frac{\partial \beta_y}{\partial y} \\ \left(\frac{\partial \beta_x}{\partial y} + \frac{\partial \beta_y}{\partial x} \right) \end{Bmatrix} \text{(Bending strains)} \quad (7)$$

$$\{\varepsilon^{nl}\} = \begin{Bmatrix} \varepsilon_x^{nl} \\ \varepsilon_y^{nl} \\ \gamma_{xy}^{nl} \end{Bmatrix} = \begin{Bmatrix} \frac{1}{2} \left(\frac{\partial w}{\partial x} \right)^2 \\ \frac{1}{2} \left(\frac{\partial w}{\partial y} \right)^2 \\ \left(\frac{\partial w}{\partial x} \frac{\partial w}{\partial y} \right) \end{Bmatrix} \text{(Nonlinear strains)} \quad (8)$$

$$\{\gamma\} = \begin{Bmatrix} \gamma_{xz} \\ \gamma_{yz} \end{Bmatrix} = \begin{Bmatrix} \frac{\partial w}{\partial x} + \beta_x \\ \frac{\partial w}{\partial y} + \beta_y \end{Bmatrix} \text{(Shear strains)} \quad (9)$$

2.4 Constitutive relations

The constitutive relationships in linear form for (FG) plate can be articulated as:

$$\begin{Bmatrix} \sigma_{xx} \\ \sigma_{yy} \\ \tau_{xy} \end{Bmatrix} = \begin{Bmatrix} C_{11} & C_{12} & 0 \\ C_{21} & C_{22} & 0 \\ 0 & 0 & C_{66} \end{Bmatrix} \begin{Bmatrix} \varepsilon_{xx} \\ \varepsilon_{yy} \\ \gamma_{xy} \end{Bmatrix} \quad (10)$$

Or

$$\{\sigma\} = [C]\{\varepsilon\} \quad (11)$$

$$\begin{Bmatrix} \tau_{xz} \\ \tau_{yz} \end{Bmatrix} = \begin{Bmatrix} k_s C_{44} & 0 \\ 0 & k_s C_{55} \end{Bmatrix} \begin{Bmatrix} \gamma_{xz} \\ \gamma_{yz} \end{Bmatrix} \quad (12)$$

where $(\sigma_{xx}, \sigma_{yy}, \tau_{xy}, \tau_{xz}, \tau_{yz})$ and $(\varepsilon_{xx}, \varepsilon_{yy}, \gamma_{xy}, \gamma_{xz}, \gamma_{yz})$ are the stresses and strains, respectively. The shear correction value $k_s = 5/6$. The rigidity coefficients C_{ij} can be formulated according to the material properties given in Eq. 2 as follows:

$$C_{11}(z) = C_{22}(z) = \frac{E(z)}{1 - \nu^2}; C_{12}(z) = C_{21}(z) = \nu \frac{E(z)}{1 - \nu^2};$$

$$C_{44}(z) = C_{55}(z) = C_{66}(z) = \frac{E(z)}{2(1 + \nu)} \quad (13)$$

2.5 Neutral surface location

The neutral surface of a plate is the surface within the thickness where no longitudinal strain occurs during bending; it experiences zero normal stress under pure bending.

To prevent the coupling of the stretching and bending effects produced by the asymmetric material characteristics of functionally graded plates with respect to the central surface, the force and moments are determined using the neutral surface position z_{Ns} , which is not coincident with the central surface of the plate, as illustrated in Fig. 3 [20]:

$$z_{ns} = z - e \quad (14)$$

In order to obtain the neutral surface position, (e) is chosen so that the membrane force caused by bending would be zero at $(z=e)$ [22].

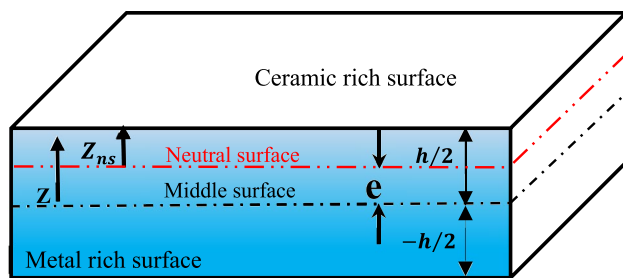


Fig. 3 Neutral surface location for the FGM plate

$$\int_{-\frac{h}{2}}^{\frac{h}{2}} \sigma_{xx} dz_{ns} = \int_{-\frac{h}{2}}^{\frac{h}{2}} \left[C_{11}(z-e) \frac{\partial \beta_x}{\partial x} + C_{12}(z-e) \frac{\partial \beta_y}{\partial y} \right] dz = 0 \quad (15)$$

By replacing Eqs. 13 into 15, we obtain:

$$\int_{-\frac{h}{2}}^{\frac{h}{2}} \frac{h}{2} \sigma_{xx} dz_{ns} = \int_{-\frac{h}{2}}^{\frac{h}{2}} \frac{h}{2} \left[\frac{E(z)}{1-v^2} \frac{\partial \beta_x}{\partial x} + v \frac{E(z)}{1-v^2} \frac{\partial \beta_y}{\partial y} \right] dz = 0 \quad (16)$$

Simplifying Eq. 16, we get:

$$\frac{1}{1-v^2} \left(\frac{\partial \beta_x}{\partial x} + v \frac{\partial \beta_y}{\partial y} \right) \int_{-\frac{h}{2}}^{\frac{h}{2}} (E(z)(z-e)) dz = 0 \quad (17)$$

Then,

$$\int_{-\frac{h}{2}}^{\frac{h}{2}} (E(z)(z-e)) dz = 0 \int_{-\frac{h}{2}}^{\frac{h}{2}} E(z) z dz - (e) \int_{-\frac{h}{2}}^{\frac{h}{2}} E(z) dz = 0 \quad (18)$$

Consequently, the neutral surface's position can be established as:

$$e = \frac{\int_{-h/2}^{h/2} E(z) z dz}{\int_{-h/2}^{h/2} E(z) dz} \quad (19)$$

2.6 Shear locking mitigation using strain-based formulations

In traditional displacement-based finite element formulations, thin plates or shells often suffer from shear locking—an artificial stiffness caused by the inability of low-order elements to accurately represent shear deformation.

To mitigate shear locking, strain-based formulations can be used instead of displacement-based ones. In strain-based formulations:

- The strain fields (including bending and shear strains) are directly assumed or approximated, rather than being derived solely from displacement fields.
- This allows for better representation of the shear deformation without enforcing overly stiff constraints.
- It improves the element's flexibility and accuracy, especially for thin or moderately thick plates.

For functionally graded material (FGM) plates analyzed with Reissner–Mindlin theory, adopting strain-based formulations helps to avoid shear locking by accurately capturing the shear strain distribution through the thickness, leading to more precise bending and shear stress predictions.

2.7 Stresses resultants

The resultant stresses M, N, and T are determined by:

$$\begin{cases} N_{xx} \\ N_{yy} \\ N_{xy} \end{cases} = \int_{-h/2}^{h/2} \begin{cases} \sigma_{xx}(z) \\ \sigma_{yy}(z) \\ \tau_{xy}(z) \end{cases} dz; \quad (20)$$

$$\begin{cases} M_{xx} \\ M_{yy} \\ M_{xy} \end{cases} = \int_{-h/2}^{h/2} \begin{cases} \sigma_{xx}(z) \\ \sigma_{yy}(z) \\ \tau_{xy}(z) \end{cases} (z-e) dz;$$

$$\begin{cases} T_{xx} \\ T_{yy} \end{cases} = \int_{-h/2}^{h/2} \begin{cases} \tau_{xz} \\ \tau_{yz} \end{cases} dz$$

Equation 20 is reformulated in the matrix form below:

$$\begin{cases} N \\ M \\ T \end{cases} = \begin{bmatrix} [A] & 0 & 0 \\ 0 & [D] & 0 \\ 0 & 0 & [A^s] \end{bmatrix} \begin{cases} \varepsilon_m \\ k \\ \gamma \end{cases} \quad (21)$$

where

$$[A] = \begin{bmatrix} A_{11} & A_{12} & 0 \\ A_{12} & A_{22} & 0 \\ 0 & 0 & A_{66} \end{bmatrix}; [D] = \begin{bmatrix} D_{11} & D_{12} & 0 \\ D_{12} & D_{22} & 0 \\ 0 & 0 & D_{66} \end{bmatrix}; [A^s] = \begin{bmatrix} A_{44}^s & 0 \\ 0 & A_{55}^s \end{bmatrix} \quad (22)$$

where A_{ij}, D_{ij}, A_{ij}^s represent the plate stiffness, as defined by:

$$A_{ij} = \int_{-h/2}^{h/2} C_{ij} dz; D_{ij} = \int_{-h/2}^{h/2} C_{ij}(z-e)^2 dz (i, j = 1, 2, 6); A_{44}^s = A_{55}^s = k_s \int_{-h/2}^{h/2} C_{44} dz \quad (23)$$

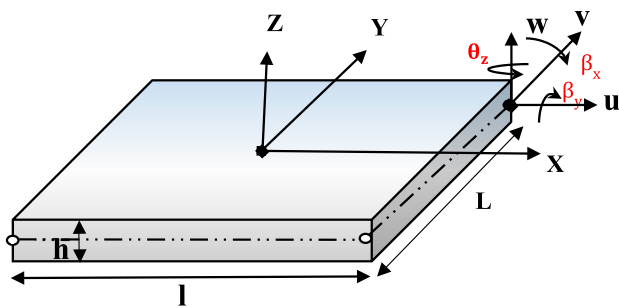


Fig. 4 Geometry of the present element SBRP24 and nodal variables

3 Finite element formulation

In this work, a new four-node rectangular Reissner–Mindlin plate element is formulated. This element is called SBRP24 (Strain-Based Rectangular Mindlin Plate with 24 unknowns) and possesses six DOFs ($u, v, \theta_z, w, \beta_x, \beta_y$) for each node, as shown in Fig. 4, corresponding to three displacements (u, v, w) in the x, y , and z directions, as well as three rotations ($\beta_x, \beta_y, \theta_z$) in the yz , xz , and xy planes, respectively.

3.1 Displacements field of the (SBRP24) element

To obtain the displacement fields for SBRP24, we combined the displacement functions derived from the thin plate element (SBRP) developed by Belouar and Guenfoud [45] and the membrane element (SBRIEIR) proposed by Sabir [30].

The displacement field defined in [30] for the stretching element (SBRIEIR) is:

$$\{U_m\} = \begin{Bmatrix} u \\ v \\ \theta_z \end{Bmatrix} = [P_m]\{\alpha_m\} \quad (24)$$

where $\{\alpha_m\}^T = \{\alpha_1, \dots, \alpha_{12}\}$

$$[P_m] \begin{bmatrix} 1 & 0 & -y & x & xy & 0 & 0 & \frac{y}{2} & 0 & \frac{y^2}{2} & xy^2 & x^2y^3 \\ 0 & 1 & x & 0 & 0 & y & xy & \frac{x}{2} & \frac{x^2}{2} & 0 & -x^2y & -x^3y^2 \\ 0 & 0 & 1 & 0 & -\frac{x}{2} & 0 & \frac{y}{2} & 0 & \frac{x}{2} & -\frac{y}{2} & -2xy & -3x^2y^2 \end{bmatrix} \quad (25)$$

The displacement functions for bending plate element (SBRP) are [45]:

$$\{U_b\} = \begin{Bmatrix} w \\ \beta_x \\ \beta_y \end{Bmatrix} = [P_b]\{\alpha_b\} \quad (26)$$

where $\{\alpha_b\}^T = \{\alpha_{13}, \dots, \alpha_{24}\}$

$$[P_b] = \begin{bmatrix} 1 & -x & -y & -\frac{x^2}{2} & -\frac{x^2y}{2} & -\frac{y^2}{2} & -\frac{xy^2}{2} & -\frac{xy}{2} & \frac{x}{2} & \frac{xy}{2} & \frac{y}{2} & \frac{xy}{2} \\ 0 & 1 & 0 & x & xy & 0 & -\frac{y^2}{2} & \frac{y}{2} & \frac{1}{2} & \frac{y}{2} & 0 & -\frac{y}{2} \\ 0 & 0 & 1 & 0 & -\frac{x^2}{2} & y & xy & \frac{x}{2} & 0 & -\frac{x}{2} & \frac{1}{2} & \frac{x}{2} \end{bmatrix} \quad (27)$$

As mentioned above, the displacement functions for the current element (SBRP24) may be obtained by combining Eqs. 25 and 27 as shown here:

$$\{U_e\} = \begin{Bmatrix} \{U_m\} \\ \{U_b\} \end{Bmatrix} = \begin{Bmatrix} u \\ v \\ \theta_z \\ w \\ \beta_x \\ \beta_y \end{Bmatrix} = \begin{bmatrix} [P_m] & 0 \\ 0 & [P_b] \end{bmatrix} \begin{Bmatrix} \{\alpha_m\} \\ \{\alpha_b\} \end{Bmatrix} = [P]\{\alpha\} \quad (28)$$

where $\{\alpha\}^T = \{\alpha_1, \dots, \alpha_{24}\}$

The 24 nodal DOFs of the element are expressed in the form of the 24 constants $\{\alpha\}$ using the transformation matrix $[C]$.

$$\{\delta^e\} = [C]\{\alpha\} \quad (29)$$

where

$$\{\delta^e\}^T = \{u_i, v_i, \theta_{zi}, w_i, \beta_{xi}, \beta_{yi}\}_{i=1,2,3,4} \quad (30)$$

$$[C] = \{[P_1][P_2][P_3][P_4]\}^T \quad (31)$$

And the matrices $[P_i]$ (for x_i, y_i from node i ($i=1, 2, 3$, and 4)) are described as:

$$[P_i] = \begin{bmatrix} [P_m]_i & 0 \\ 0 & [P_b]_i \end{bmatrix} \quad (32)$$

Using Eq. 29, we can now determine the constant values vector $\{\alpha\}$

$$\{\alpha\} = [C]^{-1}\{\delta^e\} \quad (33)$$

Then, by replacing Eqs. 33 into 28, we get:

$$\{U_e\} = [P][C]^{-1}\{\delta^e\} = [N]\{\delta^e\} \quad (34)$$

where

$$[N] = [P][C]^{-1} \quad (35)$$

3.2 Strain–displacement relations

The membrane strains $\{\varepsilon_m\}$ are calculated using Eq. 6:

$$\{\varepsilon_m\} = \begin{Bmatrix} \varepsilon_x^m \\ \varepsilon_y^m \\ \gamma_{xy}^m \end{Bmatrix} = \begin{Bmatrix} \frac{\partial}{\partial x} & 0 & 0 \\ 0 & \frac{\partial}{\partial y} & 0 \\ \frac{\partial}{\partial y} & \frac{\partial}{\partial x} & 0 \end{Bmatrix} \begin{Bmatrix} u \\ v \\ \theta_z \end{Bmatrix} \quad (36)$$

By inserting Eqs. 28 into 36, we obtain:

$$\{\varepsilon_m\} = \begin{Bmatrix} \frac{\partial}{\partial x} & 0 & 0 \\ 0 & \frac{\partial}{\partial y} & 0 \\ \frac{\partial}{\partial y} & \frac{\partial}{\partial x} & 0 \end{Bmatrix} \left[[P_m]_{3 \times 12} [0]_{3 \times 12} \right]_{3 \times 24} \{\alpha\} [Q_m]_{3 \times 24} \{\alpha\} \quad (37)$$

Using Eqs. 7 and 9, the curvature and shear strain–displacement relationship given by:

$$\{\kappa\} = \begin{Bmatrix} \kappa_x \\ \kappa_y \\ \kappa_{xy} \end{Bmatrix} = \begin{Bmatrix} 0 & \frac{\partial}{\partial x} & 0 \\ 0 & 0 & \frac{\partial}{\partial y} \\ 0 & \frac{\partial}{\partial y} & \frac{\partial}{\partial x} \end{Bmatrix} \begin{Bmatrix} w \\ \beta_x \\ \beta_y \end{Bmatrix} \quad (38)$$

$$\{\gamma\} = \begin{Bmatrix} \gamma_{xz} \\ \gamma_{yz} \end{Bmatrix} = \begin{Bmatrix} \frac{\partial}{\partial x} & 1 & 0 \\ \frac{\partial}{\partial y} & 0 & 1 \end{Bmatrix} \begin{Bmatrix} w \\ \beta_x \\ \beta_y \end{Bmatrix} \quad (39)$$

Substitution of Eqs. 28 in 38 and 39, we obtain:

$$\{\kappa\} = \begin{Bmatrix} 0 & \frac{\partial}{\partial x} & 0 \\ 0 & 0 & \frac{\partial}{\partial y} \\ 0 & \frac{\partial}{\partial y} & \frac{\partial}{\partial x} \end{Bmatrix} \left[[0]_{3 \times 12} [P_b]_{3 \times 12} \right]_{3 \times 24} \{\alpha\} = [Q_b] \{\alpha\} \quad (40)$$

$$\{\gamma\} = \begin{Bmatrix} \frac{\partial}{\partial x} & 1 & 0 \\ \frac{\partial}{\partial y} & 0 & 1 \end{Bmatrix} \left[[0]_{3 \times 12} [P_b]_{3 \times 12} \right]_{3 \times 24} \{\alpha\} = [Q_s] \{\alpha\} \quad (41)$$

The geometric strains can be formulated as [12]:

$$\{\varepsilon^g\} = \begin{Bmatrix} \frac{\partial w}{\partial x} \\ \frac{\partial w}{\partial y} \end{Bmatrix} \quad (42)$$

Substituting the transverse displacement (w) of Eqs. 27 into 42 gives:

$$\{\varepsilon^g\} = [G]\{\alpha\} \quad (43)$$

The strain–displacement relationship is obtained by replacing Eq. 33 into Eqs. (37, 40, 41), and 43, to have:

$$\{\varepsilon_m\} = [Q_m] [C]^{-1} \{\delta^e\} = [B_m] \{\delta^e\} \quad (44)$$

$$\{\kappa\} = [Q_b] [C]^{-1} \{\delta^e\} = [B_b] \{\delta^e\} \quad (45)$$

$$\{\gamma\} = [Q_s] [C]^{-1} \{\delta^e\} = [B_s] \{\delta^e\} \quad (46)$$

$$\{\varepsilon^g\} = [G] [C]^{-1} \{\delta^e\} = [B_g] \{\delta^e\} \quad (47)$$

where $[B_m]$, $[B_b]$, $[B_s]$, and $[B_g]$ are the strain–displacement matrices given by:

$$\begin{aligned} [B_m] &= [Q_m] [C]^{-1}; [B_b] = [Q_b] [C]^{-1}; \\ [B_s] &= [Q_s] [C]^{-1}; [B_g] = [G] [C]^{-1} \end{aligned} \quad (48)$$

3.3 Deduction of the elementary matrices

The normal weak formulas for bending behavior can be described as [12]:

$$\int_{\Omega} \delta \{\varepsilon_m\}^T \{N\} d\Omega + \int_{\Omega} \delta \{\kappa\}^T \{M\} d\Omega + \int_{\Omega} \delta \{\gamma\}^T \{T\} d\Omega = \int_{\Omega} \delta \{U_e\}^T \{q(x, y)\} d\Omega \quad (49)$$

where Ω is the area of the plate and $q(x, y)$ is the distributed loading force.

Substituting Eqs. (21, 34, 44, 45) and Eq. 46, into the above equation one obtains:

$$\begin{aligned} &\delta \{\delta^e\}^T \left(\int_{\Omega} [B_m]^T [D_m] [B_m] d\Omega \right) \{\delta^e\} \\ &+ \delta \{\delta^e\}^T \left(\int_{\Omega} [B_b]^T [D_b] [B_b] d\Omega \right) \{\delta^e\} \\ &+ \delta \{\delta^e\}^T \left(\int_{\Omega} [B_s]^T [D_s] [B_s] \{\delta^e\} d\Omega \right) \{\delta^e\} \\ &= \delta \{\delta^e\}^T \left(\int_{\Omega} [N]^T \{q(x, y)\} d\Omega \right) \end{aligned} \quad (50)$$

The previous equation can be formulated as follows:

$$[K_e] \{\delta^e\} = \{F_e\} \quad (51)$$

where

$$[K_e] = \int_{-b}^b \int_{-a}^a \underbrace{[B_m]^T [D_m] [B_m]}_{\text{Membrane}} + \underbrace{[B_b]^T [D_b] [B_b]}_{\text{Bending}} + \underbrace{[B_s]^T [D_s] [B_s]}_{\text{Shear}} dxdy \quad (52)$$

$$\{F_e\} = \int_{\Omega} [N]^T \{q(x, y)\} d\Omega \quad (53)$$

For free vibrational and buckling response, a variation form of the virtual work principle according to the conditions of the FSDT may be written, respectively, as [12]:

$$\begin{aligned} & \delta\{\delta^e\}^T \left(\int_{\Omega} [B_m]^T [D_m] [B_m] d\Omega \right) \{\delta^e\} \\ & + \delta\{\delta^e\}^T \left(\int_{\Omega} [B_b]^T [D_b] [B_b] d\Omega \right) \{\delta^e\} \\ & + \delta\{\delta^e\}^T \left(\int_{\Omega} [B_s]^T [D_s] [B_s] d\Omega \right) \{\delta^e\} \\ & + \delta\{\delta^e\}^T \left(\int_{\Omega} [N]^T [m] [N] d\Omega \right) \{\ddot{\delta}^e\} = 0 \end{aligned} \quad (54)$$

$$\begin{aligned} & \delta\{\delta^e\}^T \left(\int_{\Omega} [B_m]^T [D_m] [B_m] d\Omega \right) \{\delta^e\} \\ & + \delta\{\delta^e\}^T \left(\int_{\Omega} [B_b]^T [D_b] [B_b] d\Omega \right) \{\delta^e\} \\ & + \delta\{\delta^e\}^T \left(\int_{\Omega} [B_s]^T [D_s] [B_s] d\Omega \right) \{\delta^e\} \\ & + \delta\{\delta^e\}^T \left(\int_{\Omega} [B_g]^T [\bar{N}] [B_g] d\Omega \right) \{\delta^e\} = 0 \end{aligned} \quad (55)$$

where the elementary matrices for mass and geometry ($[M^e]$ and $[K_g^e]$) are defined by the following equations:

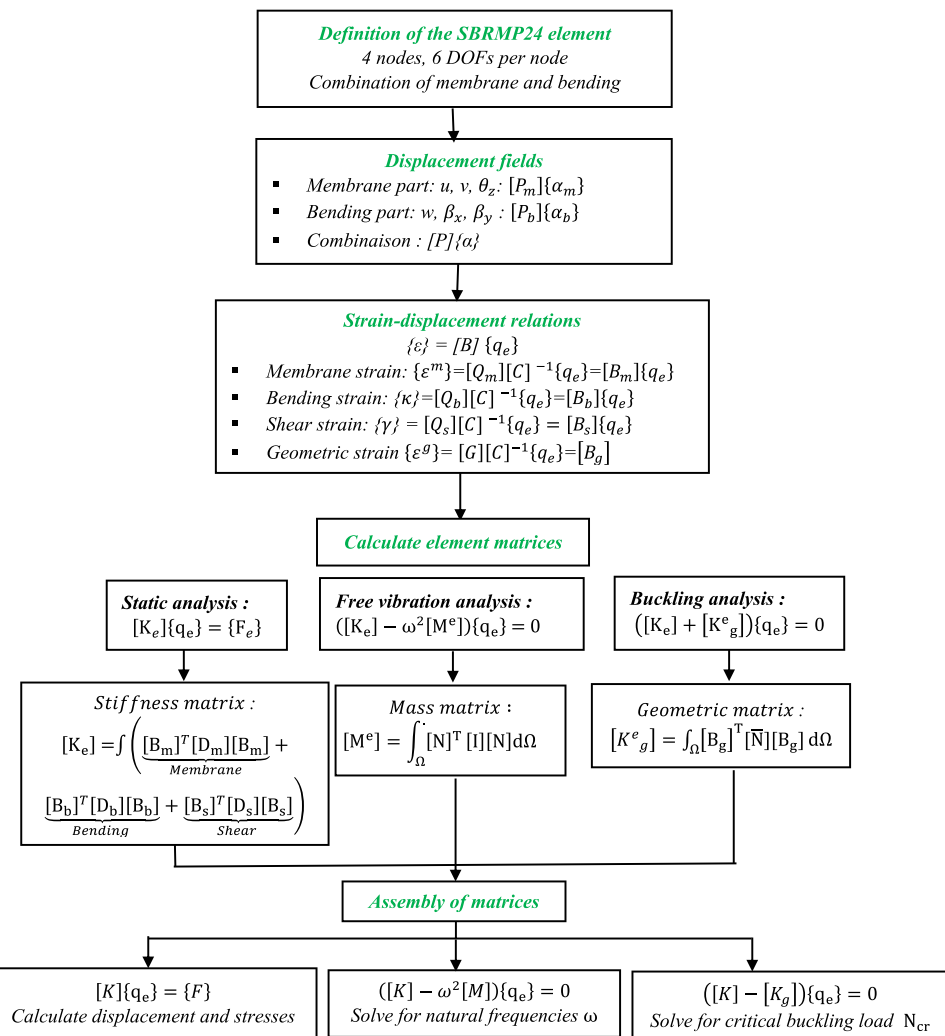
$$[M_e] = \int_{\Omega} [N]^T [m] [N] d\Omega \quad (56)$$

$$[K_g^e] = \int_{\Omega} [B_g]^T [\bar{N}] [B_g] d\Omega \quad (57)$$

in which $[m]$ and \bar{N} describe the inertia matrix and the stress matrix produced by the mechanical load, respectively, as follows:

$$[m] = \begin{bmatrix} I_0 & 0 & 0 & 0 & 0 & 0 \\ 0 & I_0 & 0 & 0 & 0 & 0 \\ 0 & 0 & 0 & 0 & 0 & 0 \\ 0 & 0 & 0 & I_0 & 0 & 0 \\ 0 & 0 & 0 & 0 & I_2 & 0 \\ 0 & 0 & 0 & 0 & 0 & I_2 \end{bmatrix} \quad (58)$$

Fig. 5 Flow diagram summarizing the steps of the finite element formulation



$$[\bar{N}] = \begin{bmatrix} N_x & N_{xy} \\ N_{xy} & N_y \end{bmatrix} \quad (59)$$

The matrices $[K_e]$, $[M_e]$, and $[K_g^e]$ and equivalent nodal load $\{F_e\}$, given in Eqs. (52, 56, 57) and (53), are calculated numerically using the Gaussian integration method. The matrices are combined through assembly to derive the rigidity, mass, and geometric matrices ($[K]$, $[M]$, and $[K_g]$) of the structure, along with the structural load vector $\{F\}$.

The following equations can be applied for the bending, free vibrational, and buckling behavior, respectively:

$$[K]\{\delta^e\} = \{F\} \quad (60)$$

$$[K] - \omega^2[M] = 0 \quad (61)$$

$$([K] - \lambda_{cr}[K_g])\{\delta^e\} = 0 \quad (62)$$

where λ_{cr} and ω are, respectively, the critical buckling loads and natural frequency.

For better understanding, a flow diagram summarizing the steps of the finite element formulation is provided in Fig. 5.

4 Results and discussion

In this part, static, free vibrational, and buckling problems are examined and analyzed to verify the convergence and efficiency of the current element (SBRP24). The assumed composition of the FG plate includes metal (aluminum, Al) and ceramic (alumina, Al_2O_3) with the specified material properties:

Metal (aluminum, Al): $E_m = 70$ Gpa; $\nu_m = 0.3$; $\rho_m = 2707$ kg/m³.

Ceramic (alumina, Al_2O_3): $E_m = 380$ Gpa; $\nu_m = 0.3$; $\rho_m = 3800$ kg/m³.

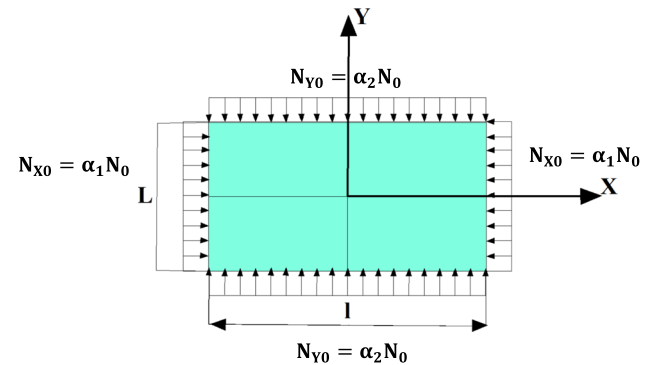
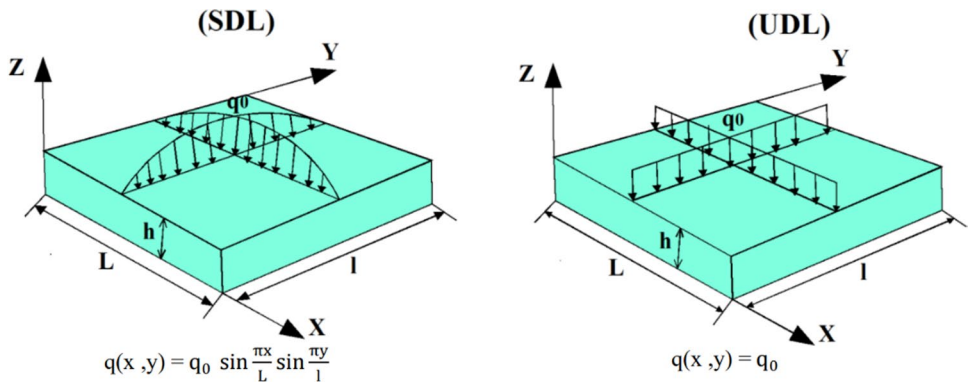
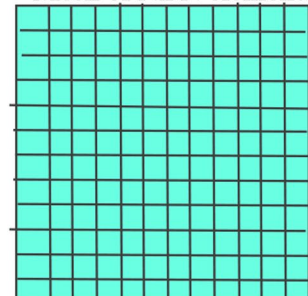


Fig. 7 Geometry and loading FGM rectangular plate

Fig. 6 Rectangular FGM plate exposed to uniform distributed load (UDL) and sinusoidal distributed load (SDL) using a mesh from $N \times N$ elements



Mesh of $N \times N$ elements



The boundary conditions for any edge of plate are listed below:

Simply supported (SSSS)

$$u = \beta_x = \theta_z = 1; v = w = \beta_y = 0 \text{ at } x = 0, 1$$

$$v = \beta_y = \theta_z = 1; u = w = \beta_x = 0 \text{ at } y = 0, L$$

Clamped (CCCC)

$$u = v = w = \beta_x = \beta_y = \theta_z = 0 \text{ at } x = 0, 1, \text{ and } y = 0, L.$$

For static loading, the plate has experienced a uniform (UDL) and sinusoidal lateral load (SDL) in the z-direction, as illustrated in Fig. 6. For the case of buckling loading, the plate has been exposed to various in-plane loading conditions, such as uniaxial compression ($\alpha_1=1, \alpha_2=0$), biaxial compression ($\alpha_1=1, \alpha_2=1$), as illustrated in Fig. 7.

For simplicity, the dimensionless formulas below are used to express deflection, in-plane stresses, natural frequencies, and critical buckling loads:

$$\begin{aligned} \bar{w} &= \frac{10h^3E_c}{L^4q_0} w\left(\frac{L}{2}, \frac{1}{2}\right); \bar{\sigma}_x \\ &= \frac{h}{q_0} \sigma_x\left(\frac{L}{2}, \frac{1}{2}, \frac{h}{2}\right); \bar{\sigma}_y \\ &= \frac{h}{q_0} \sigma_y\left(\frac{L}{2}, \frac{1}{2}, \frac{h}{3}\right); \bar{\tau}_{xy} \\ &= \frac{h}{q_0} \tau_{xy}(0,0, -\frac{h}{3}) \end{aligned} \quad (63)$$

$$\bar{\omega} = \omega h \sqrt{\frac{\rho_c}{E_c}}; \bar{\beta} = \omega h \sqrt{\frac{\rho_m}{E_m}} \quad (64)$$

$$\bar{\lambda}_{cr} = \lambda_{cr} \frac{(L^2)}{(E_m h^3)}. \quad (65)$$

4.1 Problem 1 bending analysis of SSSS FG plate.

In this problem, the static response of SSSS FG square plate is studied ($L/h=10$). The non-dimensional central displacements and stresses of the SBRP24 element evaluated for the FGM plates under uniformly distributed load ($q(x,y)=q_0$) and sinusoidally load ($q(x,y)=q_0 \sin \frac{\pi x}{L} \sin \frac{\pi y}{L}$), as illustrated in Fig. 6, are tabulated in Tables 1 and 2, respectively, using four meshes ($8 \times 8, 12 \times 12, 16 \times 16$ and 20×20) for different values of power-law index p . The results of the present

Table 1 Comparison of the dimensionless deflections and stresses in a square FG plate exposed to a uniformly distributed load with $l/h=10$

P	Mesh size	SBRP24				Tati [20]	Zenkour [15]	Reddy [13]
		8×8	12×12	16×16	20×20			
0(Ceramic)	\bar{w}	0.4421	0.4559	0.4607	0.4628	0.4663	0.4665	0.4665
	$\bar{\sigma}_x$	2.7998	2.8429	2.8566	2.8627	2.8656	2.8932	2.8920
	$\bar{\sigma}_y$	1.8665	1.8953	1.9044	1.9084	1.904	1.9103	1.9106
	$\bar{\tau}_{xy}$	1.1202	1.2060	1.2410	1.2590	1.266	1.2850	1.2855
1	\bar{w}	0.8792	0.9074	0.9169	0.9212	0.9282	0.9287	0.9421
	$\bar{\sigma}_x$	4.3254	4.3935	4.4149	4.4244	4.415	4.4745	4.2598
	$\bar{\sigma}_y$	2.1202	2.1536	2.1641	2.1687	2.164	2.1692	2.2569
	$\bar{\tau}_{xy}$	0.9671	1.0417	1.0719	1.0874	1.093	1.1143	1.1573
2	\bar{w}	1.1273	1.1634	1.1756	1.1812	1.1948	1.1940	1.2228
	$\bar{\sigma}_x$	5.0506	5.1301	5.1550	5.1661	5.155	5.2296	4.8881
	$\bar{\sigma}_y$	1.9911	2.0224	2.0322	2.0366	2.032	2.0338	2.1663
	$\bar{\tau}_{xy}$	0.8619	0.9284	0.9553	0.9691	0.9745	0.9907	1.0449
10	\bar{w}	1.4884	1.5342	1.5498	1.5570	1.5934	1.5876	1.6054
	$\bar{\sigma}_x$	7.1120	7.2195	7.2539	7.2693	7.253	7.3689	6.9540
	$\bar{\sigma}_y$	1.2625	1.2816	1.2877	1.2904	1.288	1.2820	1.3350
	$\bar{\tau}_{xy}$	0.9360	1.0075	1.0367	1.0517	1.058	1.0694	1.1119
∞ (Metal)	\bar{w}	2.3996	2.4749	2.5004	2.5121	–	2.5327	–
	$\bar{\sigma}_x$	2.7998	2.8429	2.8566	2.8627	–	2.8932	–
	$\bar{\sigma}_y$	1.8665	1.8953	1.9044	1.9084	–	1.9103	–
	$\bar{\tau}_{xy}$	1.1202	1.2060	1.2410	1.2590	–	1.2850	–

Table 2 Comparison of the dimensionless deflections and stresses in a square FG plate exposed to a sinusoidal distributed load with $l/h = 10$

P	Mesh size	SBRP24				Tati [20]	Zenkour [15]
		8×8	12×12	16×16	20×20		
0(Ceramic)	\bar{w}	0.2776	0.2857	0.2884	0.2897	0.2957	0.2960
	$\bar{\sigma}_x$	2.4494	2.1603	2.0063	1.9970	1.9570	1.9955
	$\bar{\sigma}_y$	1.6330	1.4402	1.3375	1.3111	1.3050	1.3121
	$\bar{\tau}_{xy}$	0.4100	0.4377	0.4471	0.6813	0.7025	0.7065
1	\bar{w}	0.5573	0.5738	0.5794	0.5820	0.5882	0.5889
	$\bar{\sigma}_x$	2.4067	3.3556	3.1135	3.0545	3.0240	3.0870
	$\bar{\sigma}_y$	1.8667	1.6448	1.5261	1.4834	1.4820	1.4894
	$\bar{\tau}_{xy}$	0.3614	0.3864	0.3948	0.5989	0.6066	0.6110
2	\bar{w}	0.7141	0.7353	0.7425	0.7458	0.7575	0.7573
	$\bar{\sigma}_x$	4.4450	3.9168	3.6344	3.4614	3.5320	3.6094
	$\bar{\sigma}_y$	1.7523	1.5441	1.4327	1.3946	1.3920	1.3954
	$\bar{\tau}_{xy}$	0.3216	0.3439	0.3513	0.5347	0.5406	0.5441
10	\bar{w}	0.9258	0.9524	0.9614	0.9956	1.0125	1.0089
	$\bar{\sigma}_x$	6.1817	5.4583	5.0741	4.9388	4.9690	5.0890
	$\bar{\sigma}_y$	1.0973	0.9689	0.9007	0.8790	0.8822	0.8775
	$\bar{\tau}_{xy}$	0.3353	0.3576	0.3651	0.5685	0.5868	0.5894
∞ (Metal)	\bar{w}	1.5067	1.5507	1.5656	1.5725	-	1.6070
	$\bar{\sigma}_x$	2.4494	2.1603	2.0063	1.9970	-	1.9955
	$\bar{\sigma}_y$	1.6330	1.4402	1.3375	1.3111	-	1.3121
	$\bar{\tau}_{xy}$	0.4100	0.4377	0.4471	0.6813	-	0.7065

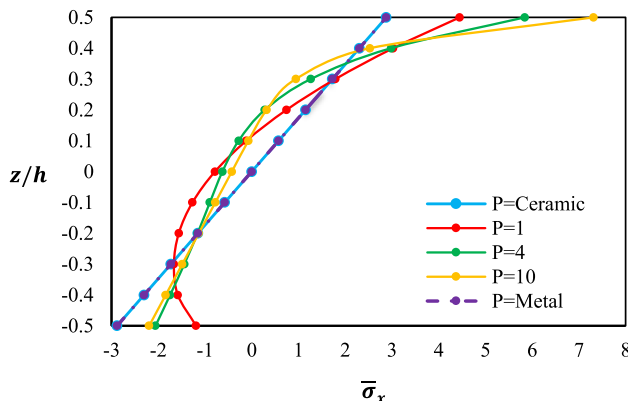


Fig. 8 Changes of the dimensionless in-plane stress ($\bar{\sigma}_x$) across the thickness of the FGM plate for different parameters p ($l/h = 10$)

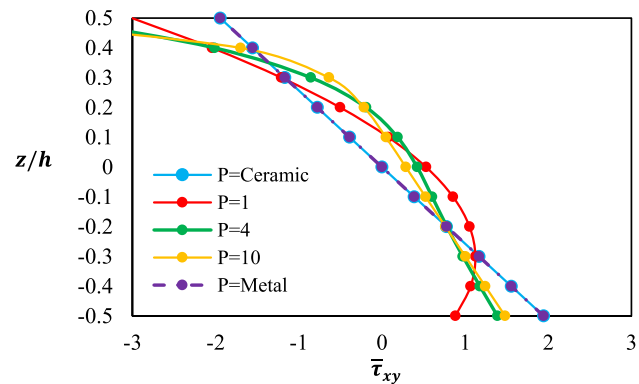


Fig. 9 Changes of the dimensionless longitudinal shear stress ($\bar{\tau}_{xy}$) across the thickness of the FGM plate for different parameters p ($l/h = 10$)

element (SBRP24) are compared with the numerical results based on HSDT presented by Tati [20], an analytical solution of Zenkour [15] using SSDT, and those obtained by Reddy [13] using TSDT.

As demonstrated in Tables 1 and 2, the results obtained using the SBRP20 element generally align well with those reported in the aforementioned references for all power-law values. It can be observed that as the power-law index (p) increases, the non-dimensional central transverse displacement (\bar{w}) and normal stress ($\bar{\sigma}_x$) both increase, while the in-plane stress ($\bar{\sigma}_y$) decreases. Additionally, the in-plane shear

stress ($\bar{\tau}_{xy}$) initially decreases as p ranges from 0 to 2 and then increases with a higher power-law index. It is noteworthy that the stresses for a fully ceramic plate are identical to those for a fully metal plate in this analysis, as both plates are considered fully homogeneous and the stresses are independent of Young's modulus.

Figures 8 and 9 show the variation in the dimensionless normal stress ($\bar{\sigma}_x$) and in-plane shear stress ($\bar{\tau}_{xy}$) across the thickness of a simply supported FG square plate subjected to a uniform distributed load (UDL), for different power-law index values (p). It is observed that the stresses in fully

Table 3 Impact of aspect ratio (l/h) on the dimensionless displacement (\bar{w}) and in-plane stress of a FGM square plate exposed to UDL

l/h	Theory	Model	\bar{w}	$\bar{\sigma}_x$	$\bar{\sigma}_y$	$\bar{\tau}_{xy}$
4	Present	FSDT	0.5837	1.1451	0.7634	0.5027
	Tati [20]	HSDT	0.5872	1.1425	0.7617	0.5070
	Zenkour [15]	SSDT	0.5865	1.1988	0.7534	0.4906
	Reddy [13]	TSDT	0.5868	1.1959	0.7541	0.4913
10	Present	FSDT	0.4628	2.8627	1.9084	1.2590
	Tati [20]	HSDT	0.4663	2.8560	1.9040	1.2660
	Zenkour [15]	SSDT	0.4665	2.8932	1.9103	1.2850
	Reddy [13]	TSDT	0.4666	2.8920	1.9106	1.2855
100	Present	FSDT	0.4374	28.4639	18.9760	12.6000
	Tati [20]	HSDT	0.4435	28.5600	19.0400	12.6500
	Zenkour [15]	SSDT	0.4438	28.7342	19.1543	13.0125
	Reddy [13]	TSDT	0.4438	28.7341	19.1543	12.9885

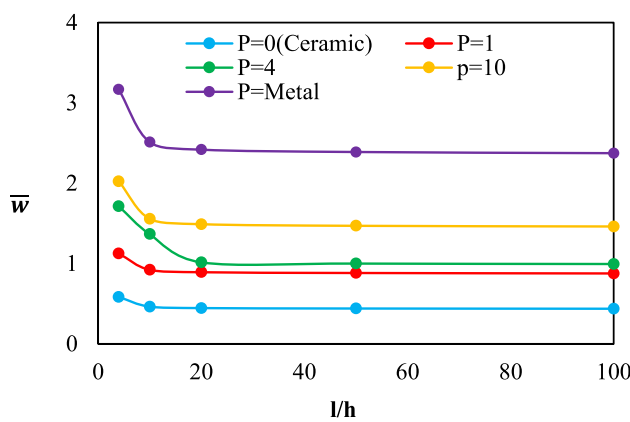


Fig. 10 Variation in the dimensionless displacement (\bar{w}) with the aspect ratio (l/h) of FG square plates

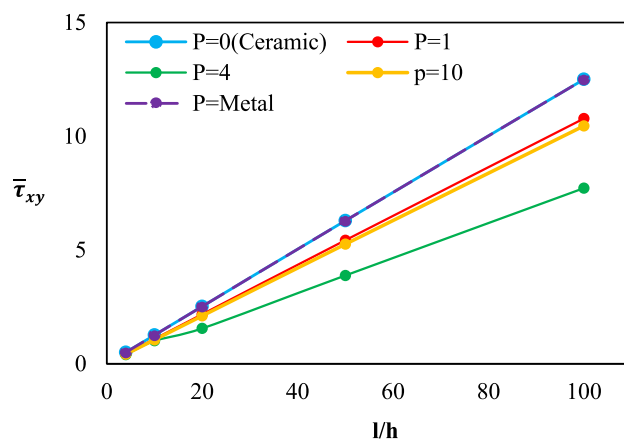


Fig. 12 Variation in the dimensionless shear stress ($\bar{\tau}_{xy}$) with the aspect ratio (l/h) of FG square plates

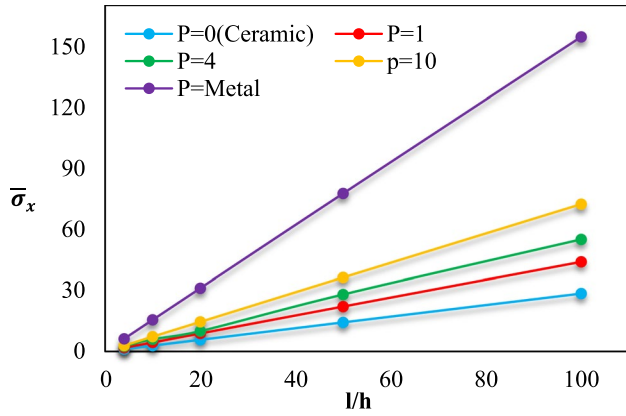


Fig. 11 Variation in the dimensionless axial stress ($\bar{\sigma}_x$) with the length/thickness ratio (l/h) of FGM square plates

ceramic and metal (homogeneous) plates are identical because they do not depend on Young's modulus. Additionally, the through-thickness distribution of in-plane

normal and shear stresses is nearly linear for isotropic plates (with $p=0$ and $p=\infty$) but becomes nonlinear for graded plates as the volume fraction index varies through the thickness.

Figure 8 illustrates that the in-plane stress ($\bar{\sigma}_x$) is tensile at the upper surface and compressive at the lower surface of the FG square plate. For $p=0$ (homogeneous ceramic material), the stress distribution is a standard linear function with the neutral plane located at $z/h=0$. The maximum compressive stresses occur at the lower edge of the plate, while the maximum tensile stresses are found at the upper edge. In contrast, the in-plane shear stress ($\bar{\tau}_{xy}$) is tensile at the lower surface and compressive at the upper surface. For the homogeneous plate, the maximum tensile shear stress is observed at the lower surface, while the minimum compressive shear stress is at the upper surface, as shown in Fig. 9.

Furthermore, the effect of the side-to-thickness ratio (l/h) on the transverse displacement and stresses of FGM plates under a uniformly distributed load with $p=0$ has

also been analyzed, as presented in Table 3. The results obtained using the present element show good agreement with those reported by Tati [20], Zenkour [15], and Reddy [13]. Table 3 also indicates that as the side-to-thickness ratio (l/h) increases, the in-plane stresses ($\bar{\sigma}_x$), ($\bar{\sigma}_y$) and ($\bar{\tau}_{xy}$) increase, while the non-dimensional transverse displacement (\bar{w}) decreases.

The variation in dimensionless displacements and stresses for various side-to-thickness ratios (l/h) and power-law index values p for the present element (SBRP24) is shown in Figs. 10, 11 and 12.

Figure 10 depicts the variation in dimensionless deflection for several gradient indexes (p) and with the different side-to-thickness ratios (l/h), respectively. It can be seen from the figure that the dimensionless deflection of FGM plates is between those of ceramic and metal, and the dimensionless deflection of metal-rich plates is higher than that of ceramic-rich plates because the Young's modulus of ceramic ($Al_2O_3 = 380$ GPa) is more than that of metal ($Al = 70$ GPa). Therefore, for the FGM plates, the dimensionless deflection increases with increasing gradient index (p). This is due to the fact that increasing the gradient index increases the volume fraction of metal, which reduces the bending stiffness of the FG plates and makes these FG plates more flexible,

resulting in larger deflection. On the other hand, it may remain unchanged as the ratio of side to thickness increases.

As shown in Fig. 11, the dimensionless normal stress ($\bar{\sigma}_x$) increase as the side-to-thickness ratio (l/h) increases and decreases as the gradient index (p) decreases.

Figure 12 illustrates the variation in dimensionless in-plane shear stress ($\bar{\tau}_{xy}$) for different side-to-thickness ratios (l/h) and gradient indices (p). The figure shows that the longitudinal shear stress ($\bar{\tau}_{xy}$) increases with the side-to-thickness ratio. Additionally, it decreases as the gradient index (p) ranges from 0 to 2 and then increases with a higher power-law index (p). This behavior is attributed to the reduction in plate stiffness.

4.2 Problem 2 free vibrational analysis of SSSS FG plate.

Consider a simply supported Al/Al₂O₃ plate with three thickness-to-side ratios ($l/h = 5, 10$ and 20) and different gradient index (p). This problem has been studied previously by a number of researchers. For example, it was investigated by Matsunaga [16] using a HSDT. Zhao et al. [41] using kip-Ritz method based on a FSDT. Belouar et al. [11] using strain approach. Hosseini-Hashemi et al.

Table 4 Dimensionless natural frequency ($\bar{\omega}$) of FG square plate with various gradient index p

l/h	Methods	P	0	0.5	1	4	10
			0	0.5	1	4	10
5	Present	0.21170	0.18096	0.16313	0.13962	0.13246	
	SBQP [11]	0.21110	0.18035	0.16296	0.13953	0.13222	
	ES-DSG [9]	0.21218	0.18114	0.16351	0.13992	0.13272	
	DSG3 [9]	0.21335	0.18216	0.16444	0.14069	0.13343	
	MITC4 [9]	0.21182	0.18082	0.16323	0.13968	0.13251	
	HSDT [16]	0.21210	0.18190	0.16400	0.13830	0.13060	
	Kip-Ritz [41]	0.20550	0.17570	0.15870	0.13560	0.12840	
	Reference [8]	0.21120	0.18050	0.16310	0.13970	0.13240	
10	Present	0.05783	0.04904	0.04424	0.03821	0.03661	
	SBQP [11]	0.05765	0.04895	0.04415	0.03819	0.03653	
	ES-DSG [9]	0.05800	0.04924	0.04439	0.03839	0.03673	
	DSG3 [9]	0.05834	0.04954	0.04467	0.03861	0.03693	
	MITC4 [9]	0.05787	0.04913	0.04429	0.03830	0.03665	
	HSDT [16]	0.05777	0.04917	0.04426	0.03811	0.03642	
	Kip-Ritz [41]	0.05673	0.04818	0.04346	0.03757	0.03591	
	Reference [8]	0.05770	0.04900	0.04420	0.03820	0.03660	
20	Present	0.01483	0.01257	0.01133	0.00983	0.00943	
	SBQP [11]	0.01479	0.01253	0.01129	0.00980	0.00941	
	ES-DSG [9]	0.01488	0.01261	0.01137	0.00986	0.00946	
	DSG3 [9]	0.01498	0.01270	0.01145	0.00993	0.00952	
	MITC4 [9]	0.01485	0.01258	0.01134	0.00984	0.00944	
	Kip-Ritz [41]	0.01464	0.01241	0.01118	0.00970	0.00931	
	Reference [8]	0.01480	0.01250	0.01130	0.00980	0.00940	

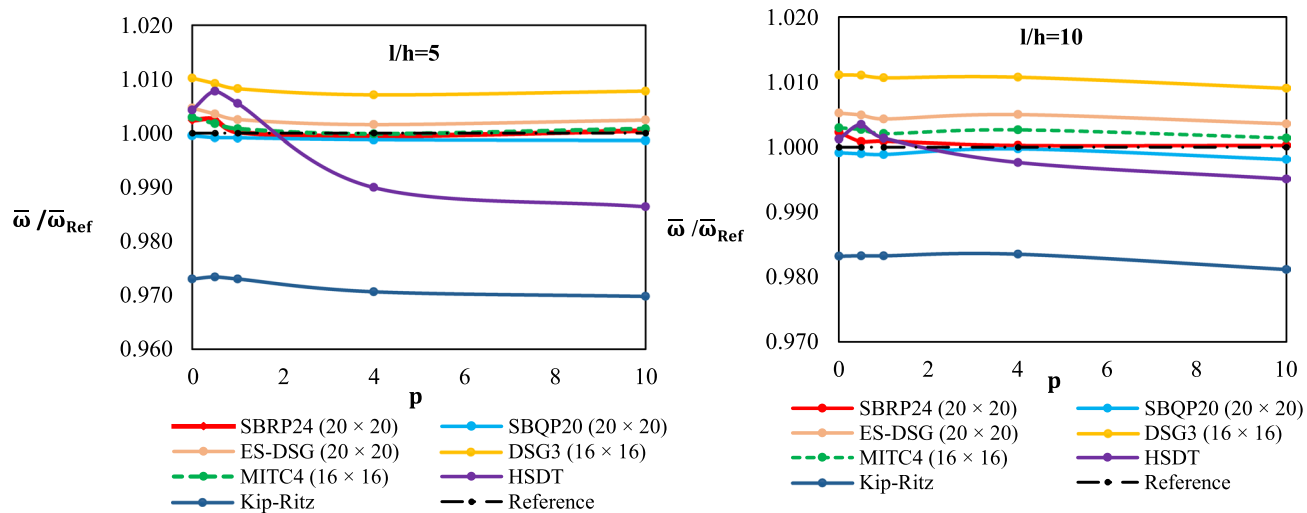


Fig. 13 Normalized frequency $\bar{\omega} / \bar{\omega}_{\text{Ref}}$ of FG square plate with various gradient index p

Table 5 Dimensionless frequencies ($\bar{\beta}$) of FG square plates for various gradient p and aspect ratios (L/l)

L/l	l/h	Theory				
		p	Present	Zaoui et al. [43]	Sadgui and Tati [22]	Jin et al. [42]
1	10	0	0.1137	0.1137	0.1136	0.1135
		1	0.0871	0.0883	0.0870	0.0870
		2	0.0791	0.0807	0.0788	0.0789
		5	0.0746	0.0756	0.0738	0.0741
		0	0.4163	0.4178	0.4156	0.4169
		1	0.3214	0.3267	0.3210	0.3222
		2	0.2913	0.2968	0.2883	0.2905
		5	0.2718	0.2725	0.2632	0.2676
		0	1.8252	1.8583	1.8224	1.8470
		1	1.4453	1.4830	1.4435	1.4687
		2	1.3040	1.3269	1.2675	1.3095
		5	1.1815	1.1576	1.0829	1.1450
		0	0.0720	0.0719	0.0722	0.0719
		1	0.0551	0.0558	0.0553	0.0550
		2	0.0500	0.0511	0.0501	0.0499
		5	0.0473	0.0480	0.0742	0.0471
		0	0.2714	0.2718	0.2721	0.2713
		1	0.2087	0.2119	0.2094	0.2088
		2	0.1893	0.1930	0.1888	0.1888
		5	0.1775	0.1788	0.1743	0.1754
		0	0.9579	1.3086	1.2943	0.9570
		1	0.7966	1.0378	1.0172	0.7937
		2	0.7195	0.9322	0.8988	0.7149
		5	0.6216	0.8250	0.7824	0.6168

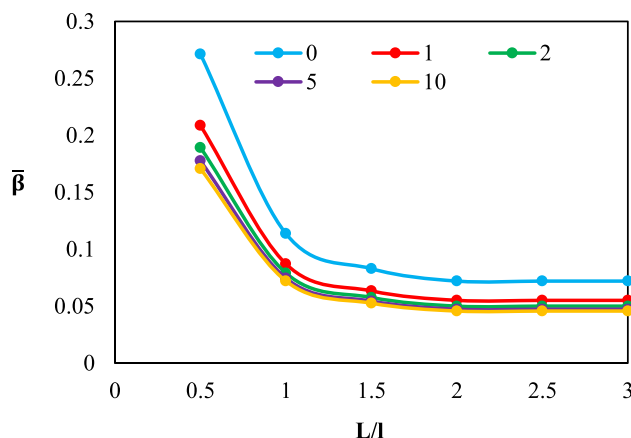


Fig. 14 Impact of aspect ratios (L/l) on the dimensionless natural frequency ($\bar{\beta}$) of FG plates for various gradient index p with ($l/h = 10$)

[8] suggested an analytical approach based on the FSDT to obtain exact solutions to the free vibration problem of Levy-type rectangular FGM plates. The obtained results of the first frequency parameter ($\bar{\omega}$) with 20×20 mesh are tabulated in Table 4.

Figures 13 illustrates the first frequency normalized to the reference value [8] for several different gradient index

(p). It can be seen that the present results converge to the analytical results and agree well with several other available ones [9, 11, 16].

Table 5 displays the comparisons of the dimensionless natural frequency ($\bar{\beta}$) obtained by the current element with the 3D precise result suggested by Jin et al. [42], the quasi-3D results presented by Zaoui et al. [43], and a new theory of trigonometric shear deformation (TSDT) developed by Sadgui and Tati [22], for various aspect ratios (L/l), length/thickness ratios (l/h), and gradient index (p). Very close agreement is observed for all conditions, from thick to thin plates. However, they are more similar to those presented by Jin et al. [42]. Part of Table 5 is also plotted in Fig. 14 for illustration purposes. Figure 14 depicts the impact of aspect ratios (L/l) on the dimensionless natural frequencies ($\bar{\beta}$). It can be seen from the figure that the dimensionless fundamental frequency decreases as aspect ratio l/L and the gradient index (p) increase.

4.3 Problem 3 buckling analysis of SSSS FGM plate.

In this problem, the validity of the current element (SBRP24) is tested for buckling behavior of the SSSS FG rectangular plate. The plate is exposed to uniaxial ($\alpha_1 = 1, \alpha_2 = 0$) and biaxial compression loads ($\alpha_1 = 1, \alpha_2 = 1$) with ($l/L = 1, 2$

Table 6 Dimensionless buckling loads ($\bar{\lambda}_{cr}$) of FG rectangular plate under uniaxial loading ($l/L = 1; l/h = 10$)

(N _{x0} , N _{y0})	Theory	$p=0$	$p=1$	$p=2$	$p=5$	$p=10$
(1,0)	Present	18.6717	9.3862	7.32015	6.0524	5.4667
	Tati [21]	18.6385	9.3696	–	6.0323	5.4435
	Thai and Choi [18]	18.5785	9.3391	7.2631	6.0353	5.4528
	Zenkour and Aljadani [45]	18.5785	9.3391	–	6.0353	5.4528
	Reddy et al. [44]	18.5400	9.2990	7.2100	5.9900	5.4200
	Present	9.3358	4.6931	3.6600	3.06623	2.7733
	Tati [21]	9.3193	4.6848	3.6379	3.01613	2.7217
	Thai and Choi [18]	9.2891	4.6701	3.6321	3.0181	2.7347
	Zenkour and Aljadani [45]	9.2892	4.6695	3.6315	3.0176	2.7264
	Reddy et al. [44]	9.2730	4.6500	3.6080	2.9980	2.7150

Table 7 Dimensionless buckling loads ($\bar{\lambda}_{cr}$) of FG rectangular plate under uniaxial loading ($l/L = 2; l/h = 10$)

(N _{x0} , N _{y0})	Theory	$p=0$	$p=1$	$p=2$	$p=5$	$p=10$
(1,0)	Present	64.5074	33.1222	25.7931	21.1109	17.7719
	Tati [21]	64.3349	33.0332	25.3409	20.0340	17.6971
	Thai and Choi [18]	64.0801	32.8901	25.3701	20.2101	17.9201
	Zenkour and Aljadani [45]	64.0842	32.4600	25.3726	20.2122	17.9227
	Reddy et al. [44]	63.7800	32.8979	24.8600	19.8400	17.7200
	Present	21.5953	10.9790	8.5556	7.0791	6.3444
	Tati [21]	21.5960	10.9800	8.4710	6.8448	6.1048
	Thai and Choi [18]	21.5051	10.9321	8.4641	6.8751	6.1481
	Zenkour and Aljadani [45]	21.5049	10.9323	8.4643	6.8749	6.1481
	Reddy et al. [44]	21.4290	10.8300	8.3450	6.7820	6.0950

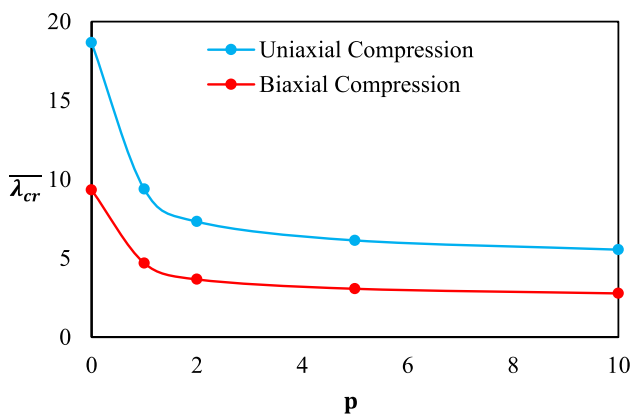


Fig. 15 Impact of the in-plane loading on the dimensionless buckling load (λ_{cr}) for a SSSS FG plate with different gradient index (p)

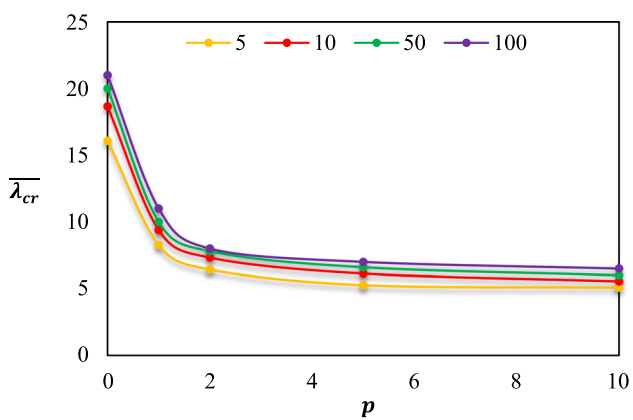


Fig. 16 Impact of the gradient index (p) on the dimensionless buckling load (λ_{cr}) exposed to uniaxial compression for a SSSS FG square plate with various aspect ratio (l/h)

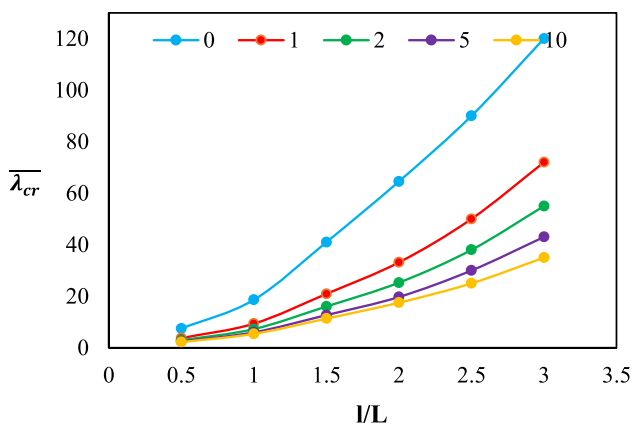


Fig. 17 Influence of aspect ratios (l/L) on the dimensionless buckling load (λ_{cr}) exposed to uniaxial compression for a SSSS FG plate with different gradient index (p)

and $l/h = 10$). The dimensionless critical buckling (λ_{cr}) load of FG plate is listed in Tables 6 and 7 using 32×16 mesh. This problem aims to investigate the impact of aspect ratios (l/L), gradient index (p), on the buckling analysis of FG plate. The comparisons of current results and those given by the analytical results are made using HSDT of Reddy et al. [44], the simple refined solution of Thai and Choi [18], the refined HSDT presented by Zenkour and Aljadani [45], and a simple (HSDT) developed by Tati [21], and a very good agreement can be found. It can be noticed from Fig. 15 that the dimensionless buckling load (λ_{cr}) is greater for uniaxial compression and less for biaxial compression. This is due to applying a tensile load to the plates, which increases bending stiffness. Furthermore, the dimensionless buckling load (λ_{cr}) reduces as the gradient index (p) value increases, and it also increases with increasing aspect ratio (l/L), as shown in Figs. 16 and 17, respectively,

A comparative table summarizing the key findings from the reviewed studies is provided for quick reference, as shown in Table 8.

5 Conclusion

This paper proposes a new four-node rectangular finite element for the static, free vibrational, and buckling behavior of FG plates using the strain approach and Reissner–Mindlin theory. The properties of the FG plate are considered to vary along the thickness direction by the power-law distributions. The notion of a neutral surface has been used to prevent the membrane-bending effect. The developed element contains six DOFs per node. It is derived by combining two elements based on the strain approach: a membrane and bending elements. The displacement fields of these elements have higher-order expressions which satisfy both rigid body modes and compatibility equations. The achieved result exhibits high agreement with the existing results in the literature for thinner to thicker plates. The conclusions that can be drawn from the results obtained for various power indices (p), thickness ratios (l/h), aspect ratios (l/L), and loading conditions are as follows:

- The present element (SBRP24) predicts excellent results for deflections and stresses when plates are exposed to static loading. The dimensionless central displacement increases as the gradient index p increases because the stiffer ceramic fraction decreases, which makes these FG plates more flexible.
- The dimensionless central displacement reduces with increasing thickness ratios, whereas the in-plane stresses increase.

Table 8 A comparative summary of the key findings from the reviewed studies

Reference	Theory	Material/structure type	Analysis type	Key findings
Zenkour [15]	SSDPT	FG plates	Static response analysis	The SBRP24 element performs exceptionally well under both uniformly distributed and sinusoidal loads, converging faster than Zenkour's analytical solution, and it also demonstrates quicker convergence compared to Reddy's analytical solution for the static response of simply supported FG square plates. Moreover, the proposed element formulation is both efficient and straightforward in predicting the bending behavior of FGM plates
Reddy [13]	TSDT	FG plates	Non-linear static and dynamic finite element results	
Tati [20]	HSDT	FG plates	bending behavior analysis	
Matsunaga [16]	2D HSDT	FG plates	Vibration, buckling	SBRP24 performs well in coupled buckling and vibrational response
Zhao et al. [41]	The element-free kp-Ritz method	FG plates	Free vibration analysis	
Sadgui and Tati [22]	HSDT	FGM plates	Vibration, stability	
Belouar et al. [11, 12]	FSDT + assumed strain FEM	FG square, skew, circular plates	Bending, vibration, buckling	
Reddy et al. [44]	HSDT	FGM plates	Buckling analysis	
Thai and Choi [18]	RPT theory	FGM plates	Buckling analysis	
Zenkour and Aljadani [45]	Refined HSDT	FGM plates	Mechanical buckling	

- It is deduced that the in-plane and shear stresses are the same for totally metallic and totally ceramic plates.
- The dimensionless natural frequencies reduce as the gradient index increases due to the reduction in stiffness of the FGM plate.
- The dimensionless natural frequencies increase as the thickness ratios increase and decrease as the aspect ratios increase.
- The dimensionless critical buckling load reduces with increasing gradient index p and increases with increasing thickness ratios and aspect ratios.
- The dimensionless critical buckling loads for the uniaxial compression are higher than for the biaxial compression.

The current finite element formulation is a promising tool for the simulation and computation of FG plates. In the future, this element will be expanded for analyzing FG plates under thermo-mechanical buckling analysis and also for FG shell structures.

Appendix

The membrane strains $\{\varepsilon_m\}$ specified in Eq. (36) satisfy the compatibility conditions as follows [29, 30]:

$$\frac{\partial^2 \varepsilon_x}{\partial y^2} + \frac{\partial^2 \varepsilon_y}{\partial x^2} - \frac{\partial^2 \gamma_{xy}}{\partial x \partial y} = 0 \quad (1a)$$

The curvatures and shear strains ($\kappa_x, \kappa_y, \kappa_{xy}, \gamma_{xz}, \gamma_{yz}$) specified in Eqs. (38) and (39) are satisfied by the compatibility equations [35–37]:

$$\begin{aligned} \frac{\partial^2 \kappa_x}{\partial y^2} + \frac{\partial^2 \kappa_y}{\partial x^2} &= \frac{\partial^2 \kappa_{xy}}{\partial x \partial y} \frac{\partial^2 \gamma_{xz}}{\partial x \partial y} - \frac{\partial^2 \gamma_{yz}}{\partial x^2} + \frac{\partial \kappa_{xy}}{\partial x} \\ &= 2 \frac{\partial \kappa_x}{\partial y} \frac{\partial^2 \gamma_{yz}}{\partial x \partial y} - \frac{\partial^2 \gamma_{xz}}{\partial y^2} + \frac{\partial \kappa_{xy}}{\partial y} \\ &= 2 \frac{\partial \kappa_y}{\partial x} \end{aligned} \quad (2a)$$

Funding The authors state that they did not receive any grants, funds, or other support while writing this article.

Declarations

Conflict of interest The authors declare that they have no conflict of interest.

References

- Fukui Y (1991) Fundamental investigation of functionally graded material manufacturing system using centrifugal force. *Int J Jpn Soc Mech Eng Ser III* 34:144–148
- Akavci SS, Tanrikulu AH (2015) Static and free vibration analysis of functionally graded plates based on a new quasi-3D and 2D shear deformation theories. *Compos Part B* 83:203–215
- Javaheri R, Eslami M (2002) Buckling of functionally graded plates under in-plane compressive loading. *J Appl Math Mech* 82:277–283
- Mohammadi M, Saidi A, Jomehzadeh E (2010) Levy solution for buckling analysis of functionally graded rectangular plates. *Appl Compos Mater* 17:81–93. <https://doi.org/10.1007/s10443-009-9100-z>
- Damanpack A, Bodaghi M, Ghassemi H, Sayehbani M (2013) Boundary element method applied to the bending analysis of thin functionally graded plates. *Lat Am J Solids Struct* 10:549–570. <https://doi.org/10.1590/S1679-78252013000300006>
- Chen CS, Chen TJ, Chien RD (2006) Nonlinear vibration of initially stressed functionally graded plates. *Thin-Walled Struct* 44(8):844–851. <https://doi.org/10.1016/j.tws.2006.08.007>
- Yuda H, Xiaoguang Z (2011) Parametric vibrations and stability of a functionally graded plate. *Mech Based Des Struct Mach* 39(3):367–377. <https://doi.org/10.1080/15397734.2011.557970>
- Hosseini-Hashemi S, Fadaee M, Atashipour SR (2011) A new exact analytical approach for free vibration of Reissner-Mindlin functionally graded rectangular plates. *Int J Mech Sci* 53:11–22
- Nguyen-Xuan H, Tran LV, Nguyen-Thoi T, Vu-Do HC (2011) Analysis of functionally graded plates using an edge-based smoothed finite element method. *Compos Struct* 93(11):3019–3039
- Bellifa H, Benrahou KH, Hadji L, Houari MS, Tounsi A (2016) Bending and free vibration analysis of functionally graded plates using a simple shear deformation theory and the concept the neutral surface position. *J Braz Soc Mech Sci Eng* 38:265–275. <https://doi.org/10.1007/s40430-015-0354-0>
- Belouar A, Boussem F, Houhou MN, Tati A, Fortas L (2022) Strain-based finite element formulation for the analysis of functionally graded plates. *Arch Appl Mech* 92(7):2061–2079. <https://doi.org/10.1007/s00419-022-02160-y>
- Belouar A, Boussem F, Tati A (2023) A novel C0 strain-based finite element for free vibration and buckling analyses of functionally graded plates. *J Vib Eng Technol* 11:281–300. <https://doi.org/10.1007/s42417-022-00577-x>
- Reddy JN (2000) Analysis of functionally graded plates. *Int J Numer Methods Eng* 47:663–684
- Zenkour AM (2004) Analytical solution for bending of crossply laminated plates under thermo-mechanical loading. *Compos Struct* 65:367–379. <https://doi.org/10.1016/j.compstruct.2003.11.012>
- Zenkour AM (2006) Generalized shear deformation theory for bending analysis of functionally graded materials. *Appl Math Model* 30:67–84
- Matsunaga H (2008) Free vibration and stability of functionally graded plates according to a 2D higher-order deformation theory. *Compos Struct* 82(4):499–512
- Talha M, Singh BN (2010) Static response and free vibration analysis of FGM plates using higher order shear deformation theory. *Appl Math Model* 34:3991–4011
- Thai H-T, Choi D-H (2012) An efficient and simple refined theory for buckling analysis of functionally graded plates. *Appl Math Model* 36(3):1008–1022. <https://doi.org/10.1016/j.apm.2011.07.062>
- Zenkour AM (2013) A simple four-unknown refined theory for bending analysis of functionally graded plates. *Appl Math Model* 37(20–21):9041–9051. <https://doi.org/10.1016/j.apm.2013.04.022>
- Tati A (2021) A five unknowns high order shear deformation finite element model for functionally graded plates bending behavior analysis. *J Braz Soc Mech Sci Eng* 43(1):1–14. <https://doi.org/10.1007/s40430-020-02736-1>
- Tati A (2021) Finite element analysis of thermal and mechanical buckling behavior of functionally graded plates. *Arch Appl Mech* 91:4571–4587. <https://doi.org/10.1007/s00419-021-02025-w>
- Sadgui A, Tati A (2021) A novel trigonometric shear deformation theory for the buckling and free vibration analysis of functionally graded plates. *Mech Adv Mater Struct* 29:6648–6663
- Zahari K, Hilali Y, Mesmoudi S, Khaoulani RE, Bourihane O (2024) Enhancing buckling analysis of functionally graded plates using unified and generalized higher-order shear deformation theories. *Mater Today Commun*. <https://doi.org/10.1016/j.mtcomm.2024.108094>
- Ashwell DG, Sabir AB (1972) A new cylindrical shell finite element based on simple independent strain functions. *Int J Mech Sci* 14(3):171–183
- Djoudi M, Bahai H (2003) A shallow shell finite element for the linear and non-linear analysis of cylindrical shells. *Eng Struct* 25:769–778
- Sabir A, Lock A (1972) A curved, cylindrical shell, finite element. *Int J Mech Sci* 14:125–135
- Sabir A, Mousa A (1996) Finite-element analysis of cylindrical-conical storage tanks using strain-based elements. *Struct Eng Rev* 4:367–374
- Belarbi MT, Maalem T (2012) On improved rectangular finite element for plane linear elasticity analysis. *Rev Eur Elem Finis* 14(8):985–997. <https://doi.org/10.3166/reef.14.985-997>
- Rebiai C, Belouar L (2013) A new strain based rectangular finite element with drilling rotation for linear and nonlinear analysis. *Arch Civ Mech Eng* 13:72–81. <https://doi.org/10.1016/j.acme.2012.10.001>
- Sabir AB (1985) A rectangular and triangular plane elasticity element with drilling degrees of freedom. In: Proceedings of the second international conference on variational methods in engineering, Vol 9, pp. 17–25
- Belarbi MT, Charif A (1999) Développement d'un nouvel élément hexaédrique simple basé sur le modèle en déformation pour l'étude des plaques minces et épaisses. *Revue Européenne des Éléments Finis* 8(2):135–157
- Belouar L, Guerraiche K (2014) A new strain based brick element for plate bending. *Alexandria Eng J* 53:95–105. <https://doi.org/10.1016/j.aej.2013.10.004>
- Messai A, Belouar L, Merzouki T (2019) Static and free vibration of plates with a strain based brick element. *Eur J Comput Mech*. <https://doi.org/10.1080/17797179.2018.1560845>
- Belouar A, Benmebarek S, Belouar L (2020) Strain based triangular finite element for plate bending analysis. *Mech Adv Mater Struct* 27(8):620–632
- Belouar A, Benmebarek S, Houhou MN, Belouar L (2019) Static, free vibration, and buckling analysis of plates using strain-based Reissner-Mindlin elements. *Int J Adv Struct Eng* 11:211–230
- Belouar A, Benmebarek S, Houhou MN, Belouar L (2020) Free vibration with Mindlin plate finite element based on the strain

- approach. *J Inst Eng India Ser C* 101:331–346. <https://doi.org/10.1007/s40032-020-00555-w>
37. Belounar L, Guenfoud M (2005) A new rectangular finite element based on the strain approach for plate bending. *Thin Walled Struct* 43:47–63. <https://doi.org/10.1016/j.tws.2004.08.003>
38. Boussem F, Belounar A, Belounar L (2022) Assumed strain finite element for natural frequencies of bending plates. *World J Eng* 19(5):620–631
39. Boussem F, Belounar L (2020) A plate bending Kirchhoff element based on assumed strain functions. *J Solid Mech* 12(4):935–952
40. Guenfoud H, Himeur M, Ziou H, Guenfoud M (2018) A consistent triangular thin flat shell finite element with drilling rotation based on the strain approach. *Int J Struct Eng* 9:191–223
41. Zhao X, Lee YY, Liew KM (2009) Free vibration analysis of functionally graded plates using the element-free kp-Ritz method. *J Sound Vib* 319:918–939. <https://doi.org/10.1016/j.jsv.2008.06.025>
42. Jin G, Su Z, Shi S, Ye T, Gao S (2014) Three-dimensional exact solution for the free vibration of arbitrarily thick functionally graded rectangular plates with general boundary conditions. *Compos Struct* 108:565–577. <https://doi.org/10.1016/j.compositesb.2018.09.051>
43. Zaoui FZ, Ouinas D, Tounsi A (2019) New 2D and quasi-3D shear deformation theories for free vibration of functionally graded plates on elastic foundations. *Compos Part B* 159:231–247. <https://doi.org/10.1016/j.compositesb.2018.09.051>
44. Reddy BS, Kumar JS, Reddy CE, Reddy KVK (2013) Buckling analysis of functionally graded material plates using higher order shear deformation theory. *J Compos* 203:1–12. <https://doi.org/10.1155/2013/808764>
45. Zenkour AM, Aljadani MH (2018) Mechanical buckling of functionally graded plates using a refined higher-order shear and normal deformation plate theory. *Adv Aircr Spacecr Sci* 5(6):615–632. <https://doi.org/10.12989/aas.2018.5.6.615>

Publisher's Note Springer Nature remains neutral with regard to jurisdictional claims in published maps and institutional affiliations.

Springer Nature or its licensor (e.g. a society or other partner) holds exclusive rights to this article under a publishing agreement with the author(s) or other rightsholder(s); author self-archiving of the accepted manuscript version of this article is solely governed by the terms of such publishing agreement and applicable law.